Tetracorder 5.27a Performance on Simulated Tanager Data

ASU Carbon Mapper Land and Oceans Team

1. Objective

This analysis compares outputs of Tetracorder 5.27a on AVIRIS-NG (ANG) data and simulated Tanager satellite data to assess what level of mineral abundance remains detectable at the 30m spatial resolution of the satellite data. We used five flightlines from Cuprite, NV (Table S1), where there is an exposed relict hydrothermal alteration system with high spectral purity that has been extensively studied (Ashley and Abrams 1980; Kruse et al 1990; Clark et al 2003; Swayze et al 2014; Thompson et al. 2018). Tetracorder results from the native 3m resolution ANG data are used as reference data; accuracy of the expert system itself is not evaluated.

2. Methods

a. Mineral detection layers

We first ran Tetracorder 5.27a on images at each scale using appropriately convolved spectral libraries as described in Hondula & Vaughn (2023). Three output layers are produced (fit, depth, and fit times depth) for each endmember, with non-zero values recorded only for grid cells where the endmember is the best fit (i.e. no data for non-detections). These values quantify the magnitude and statistical fit between normalized values of diagnostic spectral absorption features in reference library spectra and unknown spectra (Clark et al. 2003). Feature depth is usually related to spectral abundance, and fit values are used for endmember identification. Fit values range from 0 to 1, whereas the range of depth values vary by endmember. Mineral identification in the Tetracorder expert system happens independently for various spectral regions based on the differences in the processes represented by absorption features; for mineral mapping on Earth we focus on Tetracorder's Group 1μm and Group 2μm outputs. Simulated Tanager data were created using spatial and spectral resampling of the original ANG data to 30m resolution, 5nm band spacing, and a full width half maximum of 8nm. Simulated noise was added to the smoothed data based on a radiometric noise model for the Tanager sensors provided by Planet PBC.

b. Scale comparison

To compare outputs between scales, we quantified how well identifications in the 30m Tanager results corresponded to identifications in the 3m ANG data. We mosaiced result layers from each flightline then compared detection prevalence for each endmember between scales over the entire flight area, and mapped regions where mineral identifications have been validated in situ in previous studies. In order to account for differences in spectral versus spatial dominance at 30m resolution, we quantified performance accuracy separately for each endmember. We identified what level of mineral area at the finer resolution best corresponds to the pattern of detections at 30m resolution for each endmember. This resampling threshold was calculated using the maximum F1 score in precision-recall curves comparing resampling levels of ANG scale data to detections in the Tanager scale data (Fig. 1) Precision-recall curves were used instead of ROC curves because this method is more sensitive to positive class detections (Sofaer et al. 2019), which is the focus of this analysis. Mineral area was quantified as the weighted sum of binary detection layers, i.e. fractional cover of 3m detections at 30m resolution. Then, accuracy statistics were calculated from confusion matrices comparing Tanager scale detections to reference layers of ANG scale mineral detections classified using the optimum resampling threshold.

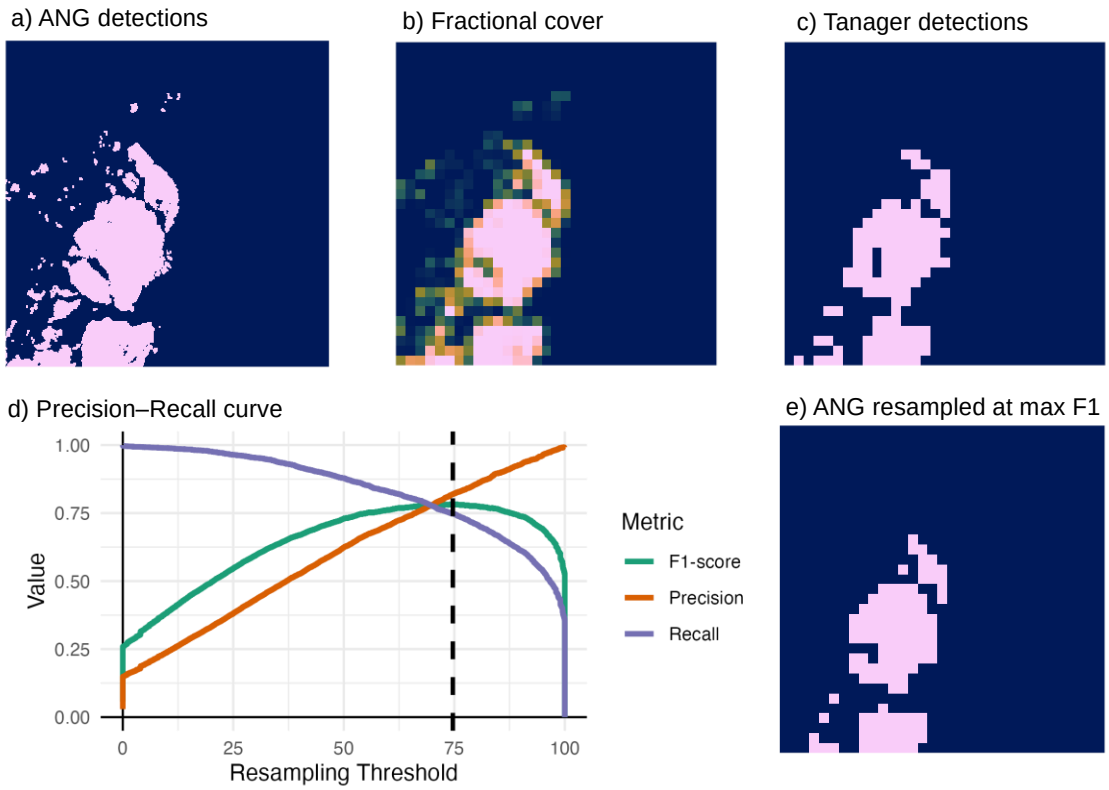

Figure 1. Method for estimating optimum resampling threshold. a) ANG 3m detections; b) fractional cover (weighted sum) of ANG detections at Tanager resolution; c) Tanager 30m detections; d) Precision-Recall curve between ANG and Tanager detections, with Tanager detections as reference class. Vertical dashed line to indicate maximum F1 score; e) ANG detections resampled to Tanager resolution using maximum F1 threshold. Panels c and e are compared to assess accuracy of Tanager scale detections, with ANG detections as reference class.

c. Mineral aggregations

Because numerous endmembers included in the Tetracorder expert system are themselves areal and/or intimate mixtures of two or more other endmembers, differences in identifications between scales are not necessarily inaccuracies. Therefore, we evaluated results for individual Tetracorder endmembers as well as for the aggregated endmember groupings described in Hondula and Vaughn (2023), i.e. pure mineral spectra only, all endmembers where a target mineral is dominant, or all endmembers where a target mineral is present. Although quantifying the performance of mixture identification is beyond the scope of this analysis, detections of several endmembers were evaluated in more detail to assess whether mixtures identified at 30m resolution generally correspond to mineral detections identified in the ANG scale data.

d. Mineral abundance

In addition to detection accuracy, we also assessed whether values in the 30m Tanager scale outputs were related to mineral abundance derived from ANG scale outputs, using seven different metrics of mineral abundance: weighted sum of detections (i.e. fractional cover), average fit (including zeros for all non-detection pixels), average feature depth (including zeros), average fit times depth (including zeros), average fit of only detections, average depth of only detections, average fit times depth of only detections.

3. Results

a. Detected minerals

For group 1µm outputs, 28 of the 69 (41%) endmembers detected at ANG scale were also detected at the Tanager scale, with good agreement in pattern and overall abundance (Fig 2a, Table 1a). More than half of the total flight area is identified as nanohematite (fe3+_hematite.nano. BR34b2b, 65%) and the next most prevalent endmembers are intimate mixtures with muscovite and goethite (fe2+_goeth+musc, 13%), secondary Fe-bearing mineral coated rocks (fe3+bearing1, 9% and fe3+mix_AMD.assemb1, 5%), and goethite coated rocks (fe3+_goethite.thincoat, 5%).

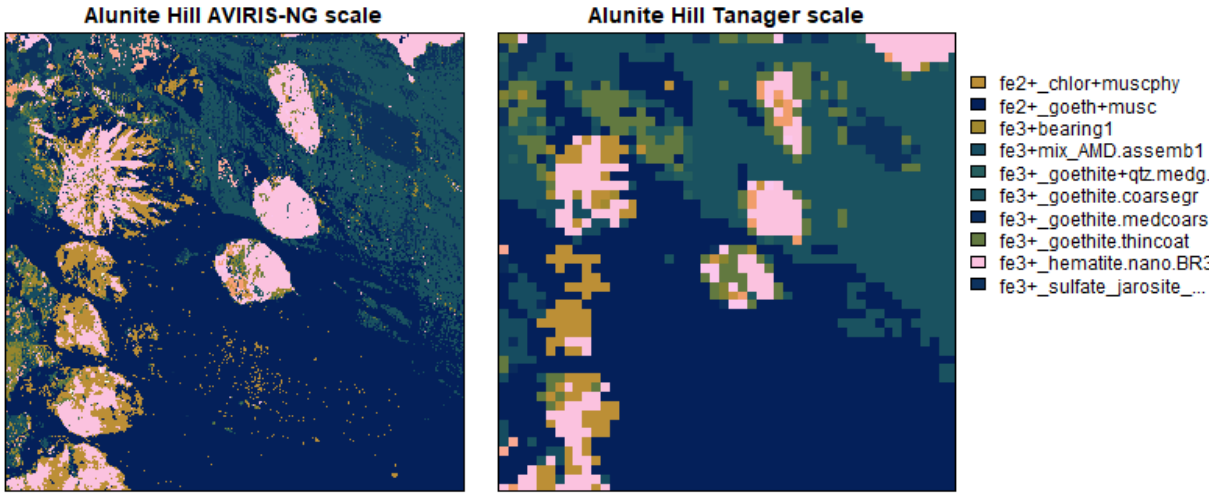

Figure 2a. Scale comparison of group 1µm endmembers in Alunite Hill area.

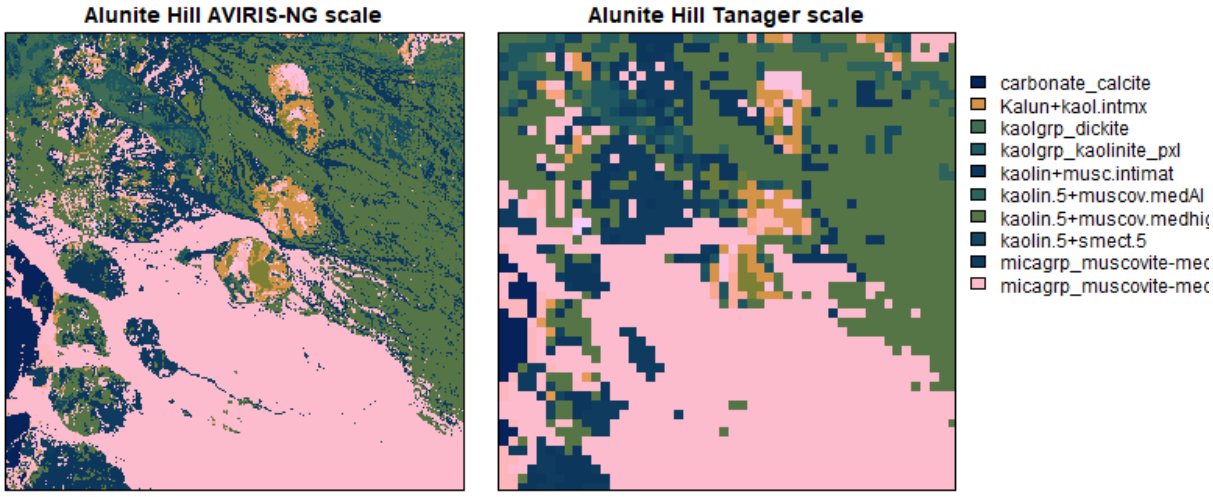

Figure 2b. Scale comparison of Group 2µm endmembers in Alunite Hill area.

For group 2µm outputs, 65 of the 131 (50%) endmembers detected at ANG scale were also detected at the Tanager scale. The most prevalent endmembers were montmorillonite (smectite_montmorillonite_ na_highswelling, 20%), intimate mixtures of kaolinite and muscovite (kaolin+musc.intimat, 15%), muscovite (micagrp_muscovite-medhigh-Al, 13%), chlorite skarn rock (chlorite-skarn, 13%), and intimate mixtures of beidellite and montmorillonite (smectite_beidellite_gds123, 10%). For both group 1 and group 2, endmembers detected at ANG scale but not at Tanager scale had low prevalence in the flight

area (<1%) and low pixel-level abundance (generally less than 10% fractional cover; Figure S1). For both Group 1 and Group 2 endmembers, there was good agreement in detection frequency across scales and more prevalent endmembers had high balanced accuracy (Fig 3). Few endmembers had higher detection frequency at Tanager scale.

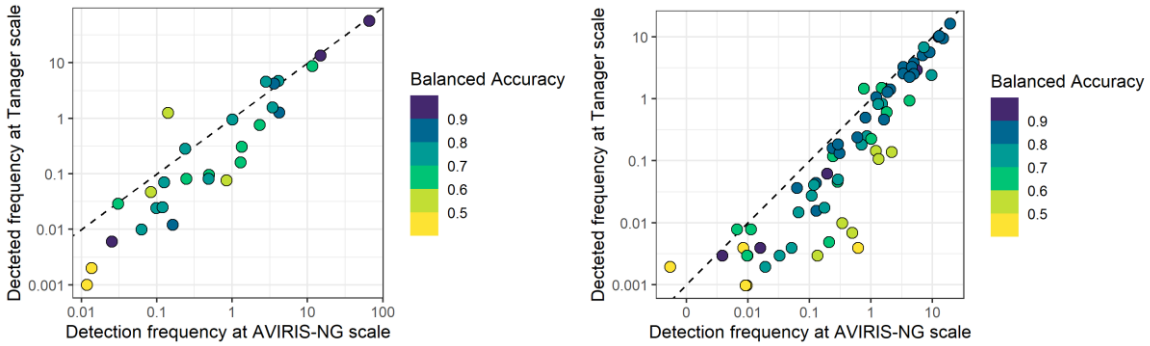

Figure 3. Detection frequency for group 1µm (left) and group 2µm (right) minerals at AVIRIS-NG scale (~3m) versus Tanager scale (30m). Dashed line is 1:1. Note that both axes are log-scaled. Marker color represents balanced accuracy.

We also evaluated ten areas of special interest that are known for having high spectral purity and/or mineral types that correspond to dominant alteration types (locations from Thompson et al 2018). Figure 4 shows carbonate calcite detections at each scale (in red) within the Quartz/Latite Dike region. See Appendix A for maps of the nine other areas.

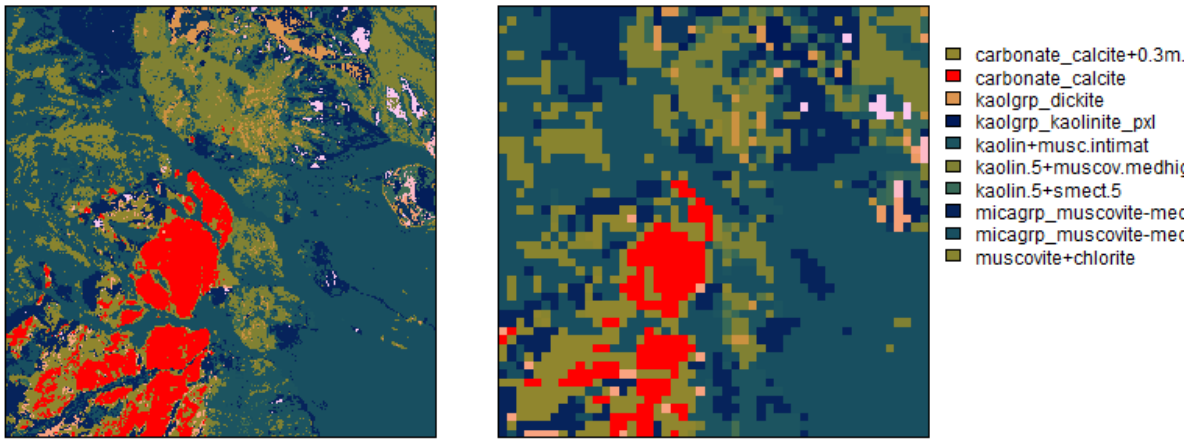

Figure 4. Quartz/Latite Dike region, with areas identified as pure calcite shown in red. Legend only shows the most abundant endmembers. See Appendix A for maps of the nine other areas of interest.

b. Detection accuracy

We calculated detection accuracy for each endmember associated with target minerals of interest based on confusion matrices comparing 30m detections to a reference of resampled 3m detections. The resampling threshold was calculated for each endmember using maximum F1 scores on a precision–recall curve, i.e. the level of resampling that best represented Tanager scale detections. Resampling thresholds averaged 51% ± 21% and ranged from 1% to 95% (Table 1).

The most prevalent endmembers generally had both high sensitivity and precision (> 50%; Fig 5, Table 2). The highest accuracy (>90%) was found for fe2+_goeth+musc, fe3+_hematite.nano.BR34b2b, carbonate_calcite, chlorite-skarn, sioh_chalcedony, and micagrp_muscovite-low-Al. Fe3+bearing1 was the most prevalent endmember with lower sensitivity (40%), however pixels with high levels of detection from ANG scale data were often categorized as other fe3+ endmembers, consistent with the known limitations on spectral uniqueness/diagnostic capability of Fe absorption features. These spectral ambiguities deflate accuracies reported at the endmember level compared to aggregated layers. Groupings also have higher accuracy because they combine mineral and mixture endmembers that may accurately reflect different Tetracorder identifications at different scales (e.g. Fig 6).

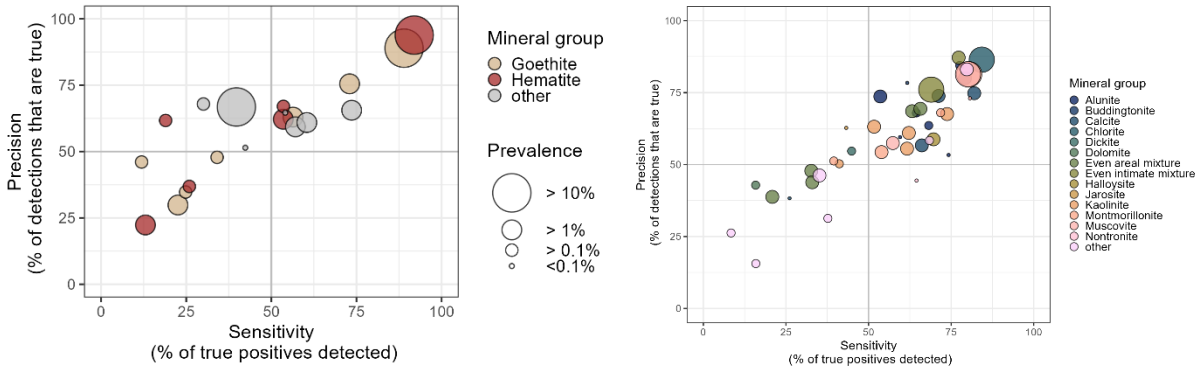

Figure 5. Accuracy metrics: Sensitivity versus precision for group 1um endmembers (left) and group 2um endmembers (right). Size of points corresponds to prevalence in the flight area (from AVIRIS-NG scale outputs). See Table 2 for a list of endmember names appearing in each quadrant.

c. Mixture detections

We evaluated fractional cover of ANG scale detections in pixels identified as mixtures at 30m Tanager scale, and found that many areas detected as pure mineral endmembers at ANG scale were identified as mixture endmembers at Tanager scale. For example, many areas with a high fractional cover of kaolinite at ANG scale were identified as areal mixtures containing kaolinite at Tanager scale (Fig 5), and areas with high fraction of carbonate calcite were identified at Tanager scale as carbonate calcite mixed with 30% muscovite. This means that accuracy reported for individual endmembers can be a conservative estimate where multiple endmember mixtures are included as possible detections in the expert system.

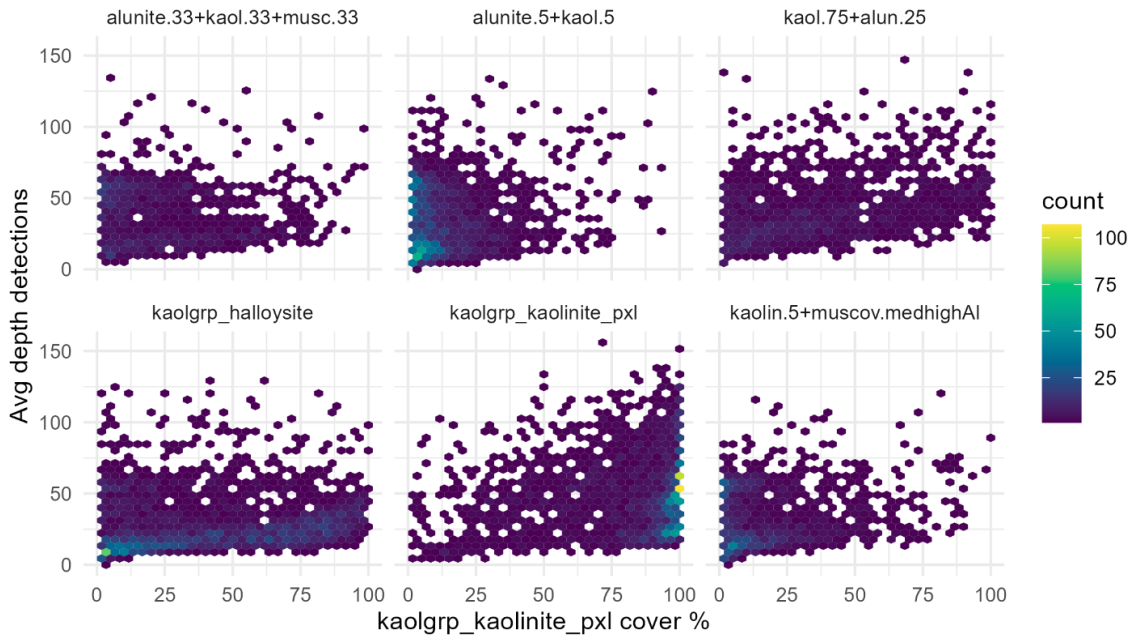

Fig 6. Kaolinite (kaolgrp_kaolinite_pxl) abundance derived from AVIRIS-NG scale data in 30m Tanager scale pixels identified as different endmembers. Shading indicates pixel count. For example, the bottom middle panel shows many pixels with near 100% percent cover of pure kaolinite (based on AVIRIS-NG scale detections) are also identified as pure kaolinite at the Tanager scale. The top middle panel shows many pixels with a low percent cover of pure kaolinite are identified as an even mixture of alunite and kaolinite.

d. Mineral abundance

For many endmembers, we also found that 30m scale results were correlated to mineral abundance in ANG scale results. The strongest linear relationships between abundance metrics at each scale were between 30m fit times depth and average fit times depth of 3m detections. Correlations and fit were highest for carbonate_calcite ($\tau = 0.83$, $R^2 = 0.94$), kaolgrp_dickite ($\tau = 0.75$, $R^2 = 0.92$), and SiOH_chalcedony ($\tau = 0.80$, $R^2 = 0.88$). Fractional cover and fit were less important in describing variability of 30m output values. Strong relationships support the use of feature depth at 30m resolution to infer mineral abundance in many cases, as planned for EMIT mission (Connelly et al 2021), especially for pure mineral and mineral plus dominant mixtures aggregation layers. For more information on interpreting spectral feature depth as a proxy for mineral abundance see (Clark et al. 2003). For the aggregations that include all endmembers with a target mineral, relationships between feature depth at each scale are lower although detection accuracy is generally higher.

4. Summary

These results generally align with previous investigations demonstrating the utility of spaceborne data for mineral detection in the Cuprite region (Kruse et al. 2003; Kruse et al 2011; Bedini and Chen 2020). We found balanced accuracy for aggregated mineral groupings was highest for alunite (93%) and lowest for dolomite (58%; Table 1d). Jarosite, dickite, and dolomite aggregations had the lowest sensitivities (45%, 45%, and 16% respectively) whereas nontronite and dolomite had the lowest precisions (44% and 43%). Mineral aggregations showed higher accuracies compared to individual endmembers, likely due to spectral and spatial mixing detections (Table 1d compared to Tables 1a and 1b; Fig. 6). Endmembers

identified in ANG data that were not detected at Tanager scale had very low fractional cover at 30m (Fig S1).

References

Ashley, R.P. and Abrams, M.J., 1980. Alteration mapping using multispectral images; Cuprite mining district, Esmeralda County, Nevada. U.S. Geological Survey Open File Report 80-367, pp. 17.

Bedini, E. and Chen, J., 2020. Application of PRISMA satellite hyperspectral imagery to mineral alteration mapping at Cuprite, Nevada, USA. *Journal of Hyperspectral Remote Sensing* v, 10(2), pp.87-94.

Clark, R.N., Swayze, G.A., Livo, K.E., Kokaly, R.F., Sutley, S.J., Dalton, J.B., McDougal, R.R. and Gent, C.A., 2003. Imaging spectroscopy: Earth and planetary remote sensing with the USGS Tetracorder and expert systems. *Journal of Geophysical Research: Planets*, 108(E12).

Connelly, D.S., Thompson, D.R., Mahowald, N.M., Li, L., Carmon, N., Okin, G.S. and Green, R.O., 2021. The EMIT mission information yield for mineral dust radiative forcing. *Remote Sensing of Environment*, 258, p.112380.

Kruse, F.A., Kierein-Young, K.S. and Boardman, J.W., 1990. Mineral mapping at Cuprite, Nevada with a 63-channel imaging spectrometer. *Photogrammetric Engineering and remote sensing*, 56.

Kruse, F.A., Boardman, J.W. and Huntington, J.F., 2003. Comparison of airborne hyperspectral data and EO-1 Hyperion for mineral mapping. *IEEE transactions on Geoscience and Remote Sensing*, 41(6), pp.1388-1400.

Kruse, F.A., Taranik, J.V., Coolbaugh, M., Michaels, J., Littlefield, E.F., Calvin, W.M. and Martini, B.A., 2011. Effect of reduced spatial resolution on mineral mapping using imaging spectrometry—Examples using Hyperspectral Infrared Imager (HyspIRI)-simulated data. *Remote Sensing*, 3(8), pp.1584-1602.

Hondula, K, and Vaughn, N. (2023). Carbon Mapper Land and Ocean Mineral Detection Algorithm GitHub Repository (v1.2.0). Zenodo. https://doi.org/10.5281/zenodo.7967293.

Sofaer, H.R., Hoeting, J.A. and Jarnevich, C.S., 2019. The area under the precision-recall curve as a performance metric for rare binary events. *Methods in Ecology and Evolution*, 10(4), pp.565-577.

Swayze, G.A., Clark, R.N., Goetz, A.F., Livo, K.E., Breit, G.N., Kruse, F.A., Sutley, S.J., Snee, L.W., Lowers, H.A., Post, J.L. and Stoffregen, R.E., 2014. Mapping advanced argillic alteration at Cuprite, Nevada, using imaging spectroscopy. *Economic Geology*, 109(5), pp.1179-1221.

Thompson, D.R., Candela, A., Wettergreen, D.S., Dobrea, E.N., Swayze, G.A., Clark, R.N. and Greenberger, R., 2018. Spatial spectroscopic models for remote exploration. *Astrobiology*, 18(7), pp.934-954.

Appendix A. Additional areas of interest. Endmembers known to be present in each area are shown in red.

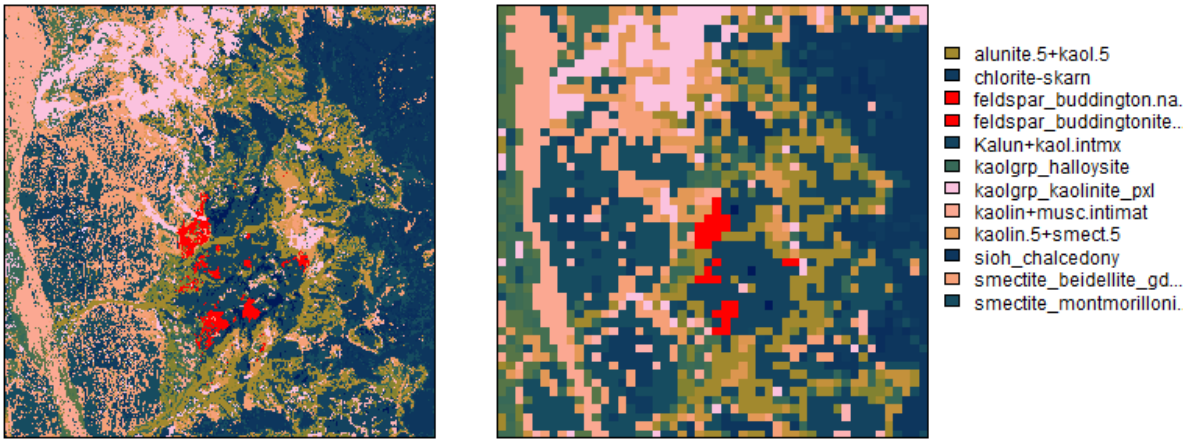

Fig A1. Buddingtonite Bump.

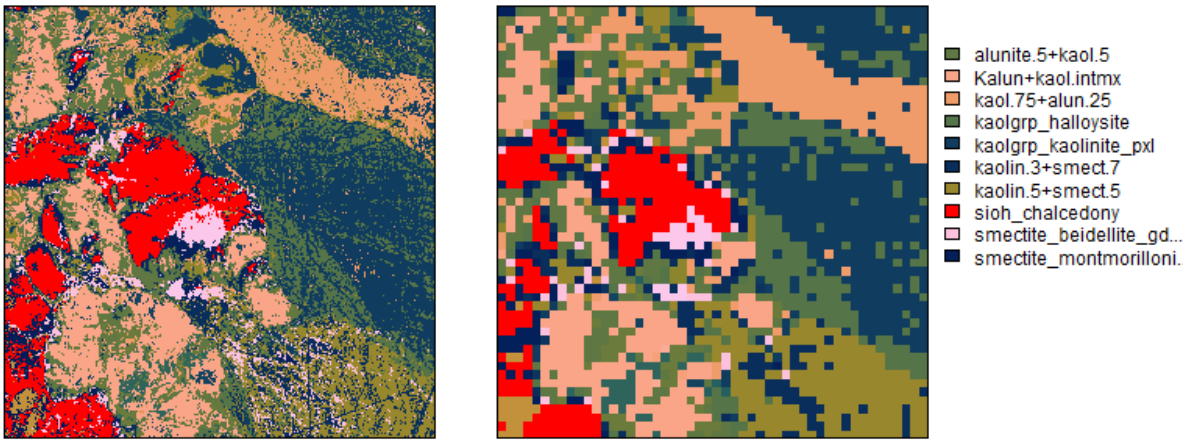

Figure A2. Opal Hill.

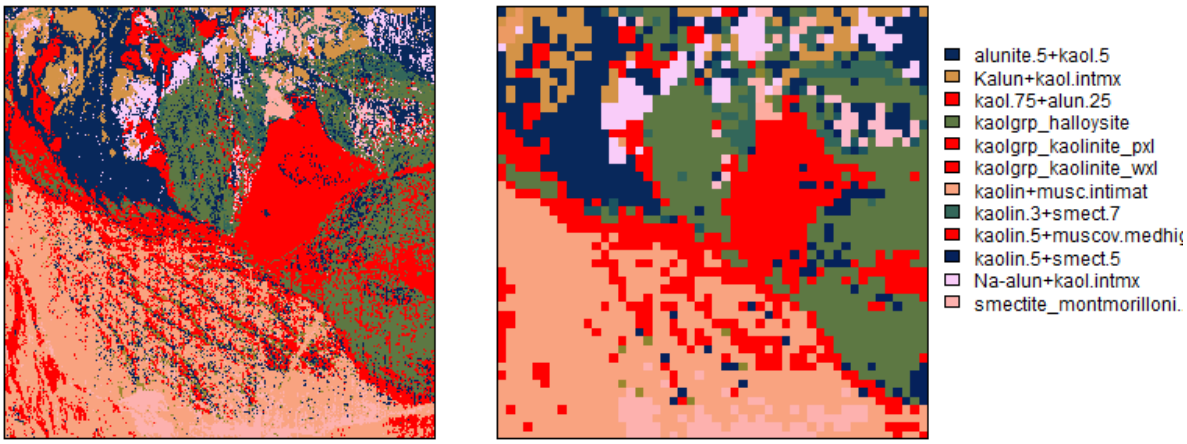

Figure A3. Kaolinite Hill.

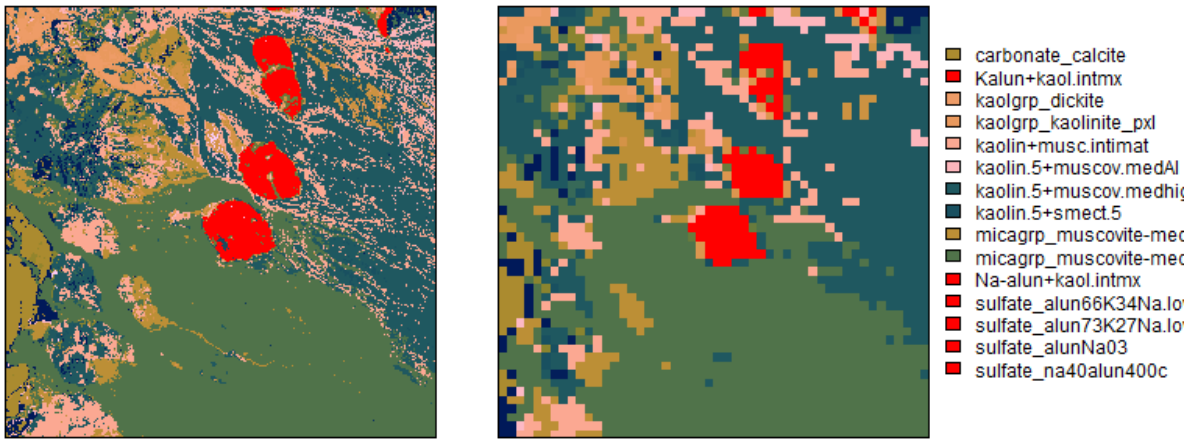

Figure A4. Alunite Hill.

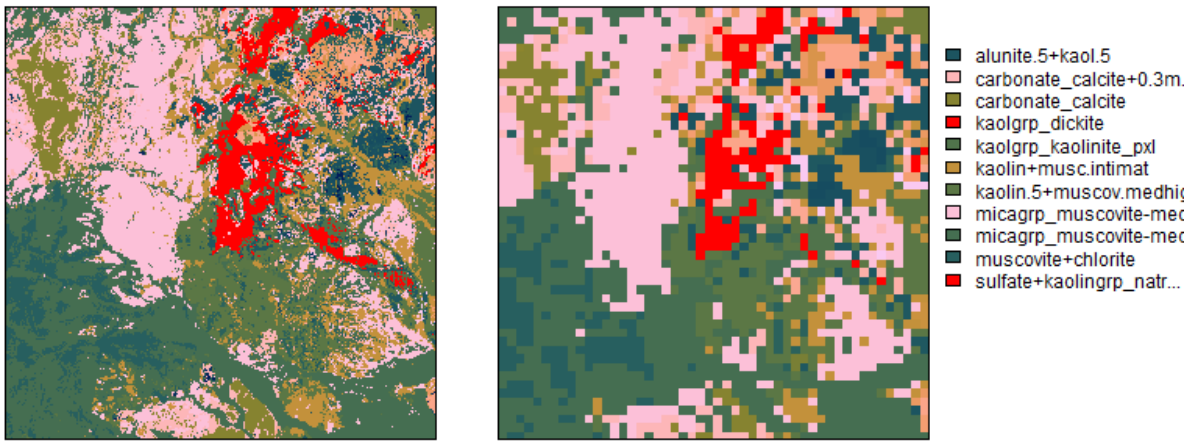

Figure A5. Dickite Ridge.

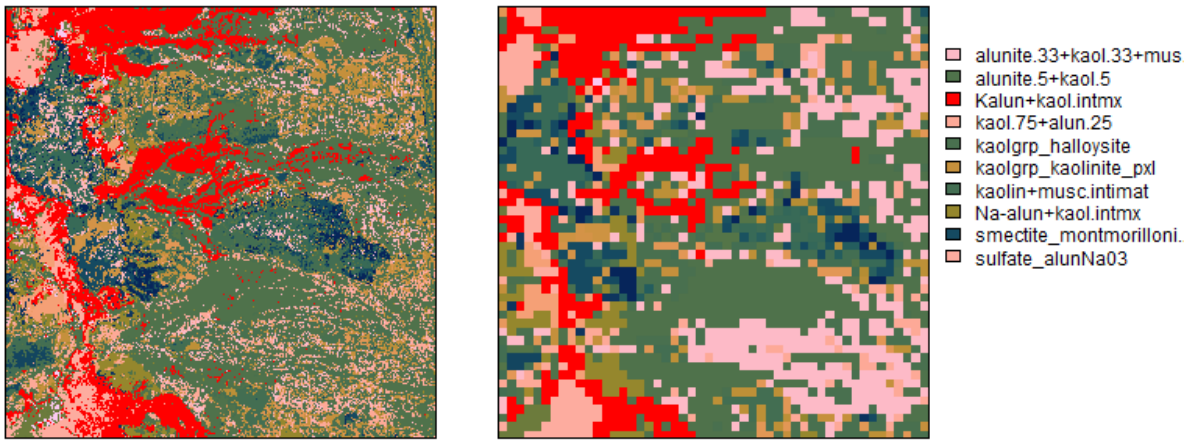

Figure A6. Pediment Basalt.

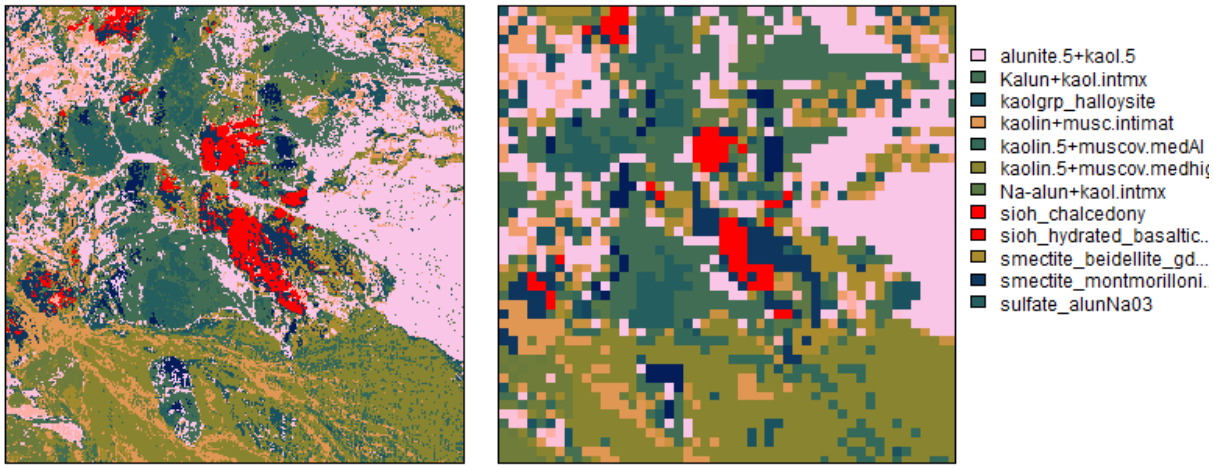

Figure A7. Opal or Chalcedony.

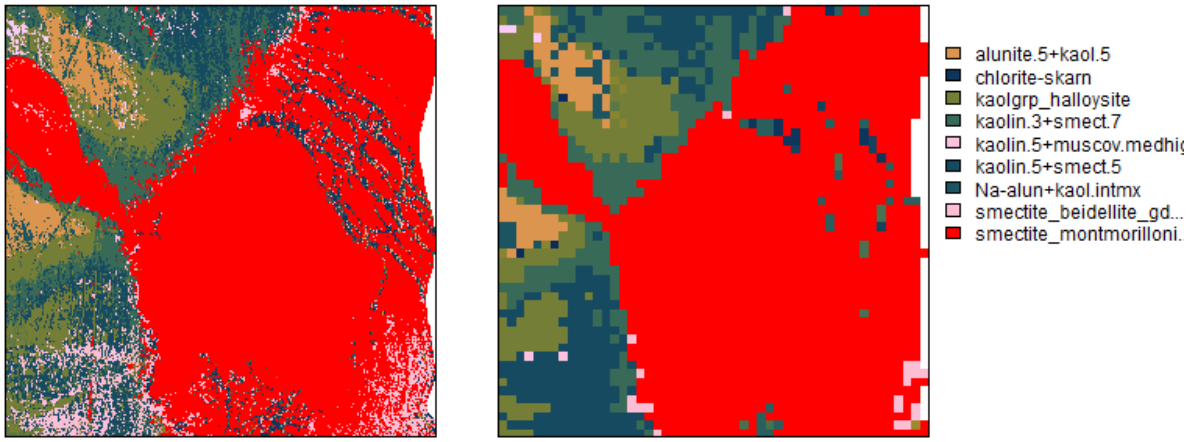

Figure A8. Stonewall Playa.

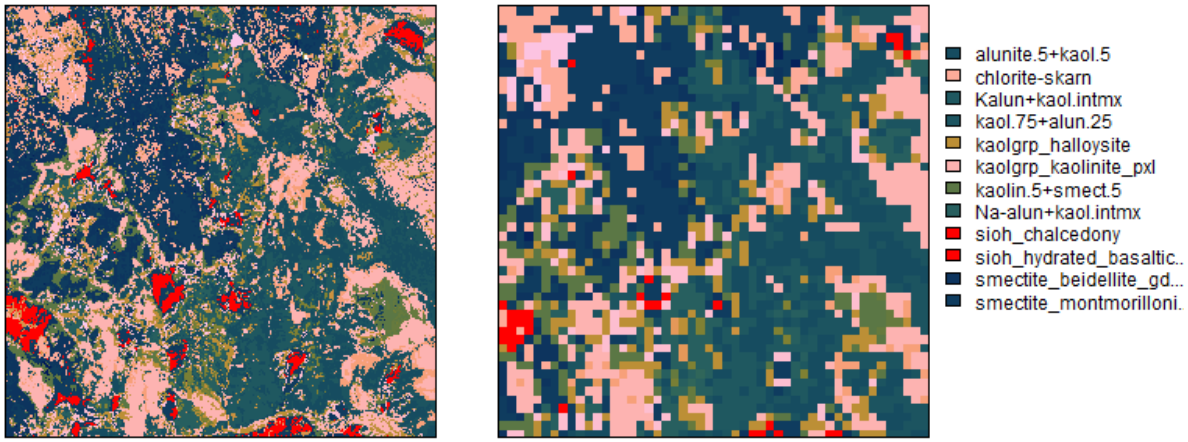

Figure A9. Three Minerals.

Tables 1a-1f report metrics of the scaling comparison for individual endmembers and layers of aggregated endmembers, sorted by prevalence within mineral groups. AVIRIS-NG and Tanager scale % are the detection prevalence across the mosaicked flight area. Resampling threshold is the pixel fractional cover that was used to classify the spatially resampled AVIRIS-NG detections in order to calculate accuracy statistics from confusion matrices. Balanced accuracy is the average of sensitivity and specificity; Sensitivity is the proportion of true positives accurately detected (a.k.a recall, or 1 minus omission error), Precision is the proportion of detections that are true positives; and specificity is the proportion of true negatives accurately detected. Accuracy metrics are only reported where N>30 Tanager scale detections.

Table 1a. Group 1um mineral endmembers

Category	Tetracorder Endmember	AVIRIS-NG scale %	Tanager scale %	Balanced Accuracy	Resampling threshold	Sensitivity	Precision
Epidote	epidote	0.01	0.00	-	-	-	-
Goethite	fe2+_goeth+musc	14.65	13.12	0.94	63.09	0.89	0.89
	fe3+_goethite.coarsegr	3.54	4.12	0.86	18.63	0.56	0.63
	fe3+_goethite.thincoat	2.75	4.46	0.77	31.14	0.73	0.76
	fe3+_goethite+qtz.medgr.gds240	2.28	0.74	0.61	56.22	0.23	0.30
	fe3+_goethite.medcoarsegr.mpc.trjar	1.32	0.30	0.62	47.66	0.25	0.35
	fe2+fe3+_chlor+goeth.propylzone	1.27	0.16	0.67	44.32	0.12	0.46
	fe3+_goethite.fingr	0.82	0.07	0.56	88.97	0.34	0.48
Hematite	fe3+_hematite.nano.BR34b2b	64.70	55.49	0.92	90.91	0.92	0.94
	fe3+_hematite.lg.gr.br34c	0.98	0.92	0.77	1.03	0.13	0.22
	fe2+fe3+mix_with_hematite_br5b	0.48	0.09	0.63	35.15	0.54	0.62
	fe3+_hematite.fine.gr.gds76	0.23	0.27	0.77	23.86	0.54	0.67
	fe3+_hematite.nano.BR34b2	0.14	1.22	0.56	17.32	0.19	0.62
	fe3+_hematite.fine.gr.fe2602	0.12	0.02	0.76	56.57	0.26	0.37
	fe3+_hematite.lg.gr.br25a	0.08	0.05	0.59	13.03	0.25	0.48

	fe3+_hematite.lg.gr.br25c	0.06	0.01	-	-	-	-
	fe3+_hematite.med.gr.br25b	0.03	0.03	-	-	-	-
other	fe3+bearing1	11.40	8.55	0.68	31.70	0.40	0.67
	fe2+_chlor+muscphy	4.14	1.25	0.87	31.35	0.57	0.59
	fe3+mix_AMD.assemb1	4.04	4.63	0.78	72.95	0.60	0.61
	fe3+_sulfate_jarosite_br34a2	3.37	1.53	0.80	87.63	0.74	0.66
	mn2+_rhodonite	0.48	0.08	0.77	2.32	0.00	0.00
	fe3+_sulfate_kjarosite200	0.24	0.08	0.65	40.59	0.30	0.68
	fe2+generic_carbonate_siderite1	0.16	0.01	-	-	-	-
	ree_samarium_oxide	0.12	0.07	0.71	26.08	0.42	0.51
	fe2+generic_brd.br36a_chlorite	0.10	0.02	-	-	-	-
	fe2+generic_vbroad_br20	0.03	0.01	-	-	-	-
	fe2+generic_nrw.cummingtonite	0.01	0.00	-	-	-	-

Table 1b. Group 2um mineral endmembers

Category	Tetracorder Endmember	AVIRIS-NG scale %	Tanager scale %	Balanced Accuracy	Resampling threshold	Sensitivity	Precision
Alunite	Kalun+kaol.intmx	3.46	2.59	0.89	63.72	0.79	0.80
	Na-alun+kaol.intmx	1.35	0.84	0.77	41.75	0.54	0.74
	sulfate_alunNa03	0.84	0.51	0.89	63.65	0.78	0.84
	sulfate_alun66K34Na.low	0.32	0.13	0.87	56.76	0.74	0.53
	sulfate_na40alun400c	0.30	0.19	0.82	50.73	0.64	0.68

	sulfate+kaolingrp_natroalun+dickite	0.24	0.16	0.84	43.19	0.68	0.64
	sulfate_kalun150c	0.18	0.02	-	-	-	-
	sulfate_kalun250c	0.12	0.04	0.80	51.58	0.60	0.60
	sulfate_alun73K27Na.low	0.11	0.03	-	-	-	-
	sulfate_na82alun100c	0.02	0.00	-	-	-	-
	sulfate_alun35K65Na.low	0.00	0.00	-	-	-	-
Buddingtonite	feldspar_buddington.namont2	0.06	0.04	0.81	56.02	0.62	0.78
	feldspar_buddingtonite_ammonium	0.01	0.00	-	-	-	-
Calcite	carbonate_calcite+0.3muscovite	7.06	5.12	0.85	53.50	0.71	0.74
	carbonate_calcite	5.69	2.94	0.91	74.67	0.82	0.75
	calcite+0.2Na-mont	3.46	3.30	0.82	46.83	0.66	0.57
	carbonate_calcite+0.2Ca-mont	0.30	0.05	0.63	48.67	0.26	0.38
	carbonate_calcite+0.2kaolwxl	0.01	0.00	-	-	-	-
Chlorite	chlorite-skarn	12.77	10.20	0.91	64.41	0.84	0.86
	chlorite_clinochlore.fe.sc-cca-1	0.01	0.00	-	-	-	-
	chlorite_clinochlore.fe.gds157	0.00	0.00	-	-	-	-
Dickite	kaolgrp_dickite	0.89	0.26	0.72	60.19	0.45	0.55
Dolomite	carbonate_dolomite	1.23	0.15	0.58	41.98	0.16	0.43
Epidote	epidote	0.01	0.00	-	-	-	-
Even areal mixture	kaolin.5+muscov.medhighAl	9.18	5.74	0.81	63.58	0.63	0.69
	alunite.5+kaol.5	5.09	3.85	0.82	54.58	0.66	0.69

	kaolin.5+muscov.medAl	1.85	0.62	0.60	41.46	0.21	0.39
	carbonate_dolomite.5+Na-mont.5	1.54	1.52	0.66	20.64	0.33	0.44
	alunite.33+kaol.33+musc.33	0.78	1.49	0.66	11.23	0.33	0.48
	calcite+0.5Ca-mont	0.14	0.00	-	-	-	-
	pyroph.5+alunit.5	0.13	0.02	-	-	-	-
	alunite.5+musc.5	0.01	0.01	-	-	-	-
Even intimate mixture	kaolin+musc.intimat	15.36	9.66	0.83	76.57	0.69	0.76
	muscovite+chlorite	1.25	1.08	0.89	42.63	0.77	0.87
Halloysite	kaolgrp_halloysite	4.71	3.31	0.84	59.00	0.70	0.59
Jarosite	sulfate_jarosite-lowT	0.30	0.05	0.72	57.41	0.43	0.63
	sulfate_jarosite-K	0.02	0.00	-	-	-	-
Kaolinite	kaolgrp_kaolinite_pxl	5.13	2.57	0.86	80.29	0.74	0.68
	kaolin.5+smect.5	4.37	2.27	0.81	55.40	0.62	0.61
	kaol.75+alun.25	2.09	1.45	0.80	47.60	0.62	0.56
	kaolin.3+smect.7	1.56	0.85	0.76	47.54	0.52	0.63
	kaolgrp_kaolinite_wxl	0.72	0.18	0.71	62.29	0.41	0.50
Montmorillonite	smectite_montmorillonite_na_highswelling	19.86	16.51	0.88	57.70	0.80	0.81
	smectite_beidellite_gds123	9.86	2.45	0.76	79.20	0.54	0.54
	smectite_montmorillonite_ca_swelling	1.67	0.47	0.86	68.06	0.72	0.68
	smectite_beidellite_gds124	0.51	0.01	-	-	-	-
	calcite.25+dolom.25+Na-mont.5	0.25	0.12	0.70	38.08	0.39	0.51

Muscovite	micagrp_muscovite-medhigh-Al	13.28	10.44	0.89	67.01	0.80	0.81
	micagrp_muscovite-med-Al	7.42	6.94	0.77	40.15	0.57	0.57
	micagrp_muscovite-low-Al	0.20	0.06	0.90	70.93	0.81	0.73
	musc+pyroph	0.01	0.01	-	-	-	-
Nontronite	smectite_nontronite_swelling	0.13	0.04	0.82	54.83	0.65	0.44
Other	hydroxide_brucite	4.33	0.95	0.67	65.00	0.35	0.46
	zoisite	2.23	0.14	0.54	45.21	0.08	0.26
	sioh_chalcedony	1.91	1.30	0.90	66.25	0.80	0.83
	palygorskite	1.37	0.11	0.58	49.48	0.16	0.16
	micagrp_paragonite	1.04	0.23	0.69	51.42	0.38	0.31
	micagrp_margarite	0.63	0.00	-	-	-	-
	sioh_hydrated_basaltic_glass	0.61	0.24	0.84	57.31	0.68	0.58
	nitrate_niter	0.35	0.01	-	-	-	-
	organic_plastic-vinyl	0.22	0.00	-	-	-	-
	organic_drygrass+.17Na-mont	0.07	0.01	-	-	-	-
	organic_vegetation-dry-grass-golden	0.05	0.00	-	-	-	-
	carbonate_aragonite	0.03	0.00	-	-	-	-
	zeolite_natrolite	0.01	0.00	-	-	-	-

Table 1c. Aggregated layers for pure mineral spectra

Category	**Tetracorder Endmember**	**AVIRIS-NG scale %**	**Tanager scale %**	**Balanced Accuracy**	**Resampling threshold**	**Sensitivity**	**Precision**

Group 1	Hematite minerals	66.36	58.03	0.92	88.30	0.93	0.94
	Goethite minerals	5.43	4.59	0.84	48.35	0.70	0.67
	Epidote minerals	0.02	0.00	-	-	-	-
Group 2	Montmorillonite minerals	20.66	16.96	0.89	59.63	0.81	0.82
	Muscovite minerals	13.48	10.51	0.89	67.86	0.80	0.81
	Calcite minerals	5.69	2.94	0.91	74.67	0.82	0.75
	Kaolinite minerals	5.48	2.73	0.85	78.76	0.71	0.72
	Halloysite (just 1 endmember)	4.71	3.31	0.84	59.00	0.70	0.59
	Alunite minerals	1.31	0.74	0.88	66.96	0.76	0.82
	Dolomite minerals	1.23	0.15	0.58	41.98	0.16	0.43
	Dickite minerals	0.89	0.26	0.72	60.19	0.45	0.55
	Jarosite minerals	0.31	0.05	0.73	57.41	0.45	0.64
	Nontronite (just 1 endmember)	0.13	0.04	0.82	54.83	0.65	0.44
	Chlorite minerals	0.08	0.01	-	-	-	-
	Buddingtonite minerals	0.06	0.04	0.81	56.02	0.62	0.78
	Epidote (just 1 endmember)	0.01	0.00	-	-	-	-

Table 1d. Aggregated layers of pure mineral spectra & mixtures where target mineral is dominant. Even mixtures contain equal fractions of two or more target minerals.

Category	**Tetracorder Endmember**	**AVIRIS-NG scale %**	**Tanager scale %**	**Balanced Accuracy**	**Resampling threshold**	**Sensitivity**	**Precision**
Group 1	Hem min + dom mixtures (same as all)	67.51	59.12	0.92	84.24	0.92	0.95
	Goethite minerals + dominant mixtures	9.13	9.91	0.85	35.59	0.73	0.76

	Epidote minerals	0.02	0.00	-	-	-	-
Group 2	Montmor. minerals + dominant mixtures	26.80	19.43	0.90	75.11	0.84	0.82
	Muscovite minerals + dominant mixtures	24.34	22.26	0.89	49.39	0.81	0.85
	Even areal mixtures	17.58	12.98	0.79	54.68	0.64	0.67
	Even intimate mixtures	17.04	10.95	0.82	68.55	0.67	0.79
	Calcite minerals +dominant mixtures	9.16	6.28	0.84	61.44	0.69	0.69
	Kaolinite minerals + dominant mixtures	11.33	7.14	0.84	66.11	0.71	0.76
	Alunite minerals + dominant mixtures	5.29	4.21	0.93	67.80	0.87	0.85
	Dolomite minerals + dominant mixtures	1.23	0.15	0.58	41.98	0.16	0.43
	Dickite minerals + dominant mixtures	0.89	0.26	0.72	60.19	0.45	0.55
	Jarosite minerals + dominant mixtures	0.32	0.05	0.72	57.41	0.45	0.64
	Nontronite (just 1 endmember)	0.13	0.04	0.82	54.83	0.65	0.44
	Chlorite minerals + dominant mixtures	12.85	10.20	0.91	64.41	0.84	0.86
	Budd min + mixtures (same as all ems)	0.07	0.04	0.80	63.19	0.60	0.74
	Epidote (just 1 endmember)	0.01	0.00	-	-	-	-

Table 1e. Aggregated layers of endmembers where target mineral is present at any level.

Category	**Tetracorder Endmember**	**AVIRIS-NG scale %**	**Tanager scale %**	**Balanced Accuracy**	**Resampling threshold**	**Sensitivity**	**Precision**
Group 1	Hem min + dom mixtures (same as all)	67.51	59.12	0.92	84.24	0.92	0.95

	Any goethite	22.68	23.18	0.91	43.50	0.86	0.88
	Epidote minerals	0.02	0.00	-	-	-	-
Group 2	Montmorillonite (any)	30.85	24.14	0.88	66.52	0.82	0.82
	Muscovite (any)	43.75	40.17	0.91	61.12	0.88	0.90
	Calcite (any)	13.36	11.21	0.93	58.56	0.89	0.81
	Kaolinite (any)	38.56	30.85	0.87	70.78	0.79	0.89
	Halloysite (just 1 endmember)	4.71	3.31	0.84	59.00	0.70	0.59
	Alunite (any)	10.62	10.71	0.92	45.45	0.86	0.87
	Dolomite (any)	3.17	1.79	0.62	31.16	0.26	0.37
	Dickite (any)	1.08	0.40	0.82	65.71	0.64	0.52
	Jarosite (any)	0.33	0.05	0.76	64.42	0.52	0.53
	Nontronite (just 1 endmember)	0.13	0.04	0.82	54.83	0.65	0.44
	Chlorite (any)	14.10	11.28	0.91	64.41	0.85	0.85
	Budd min + mixtures (same as all ems)	0.07	0.04	0.80	63.19	0.60	0.74
	Epidote (just 1 endmember)	0.01	0.00	-	-	-	-
	Pyrophyllite (any)	0.15	0.02	-	-	-	-

Table 1f. Other aggregation layers defined in Tetracorder 5.27a

Category	**Tetracorder Endmember**	**AVIRIS-NG scale %**	**Tanager scale %**	**Balanced Accuracy**	**Resampling threshold**	**Sensitivity**	**Precision**
Group 1	fe2generic	0.14	0.03	0.74	71.61	0.48	0.68
	hematite_nano	66.29	57.81	0.92	84.72	0.92	0.95

	hematite_fine	0.35	0.31	0.72	24.52	0.44	0.70
	hematite_med	0.03	0.03	-	-	-	-
	hematite_large	1.08	0.99	0.77	35.15	0.54	0.64
	hematite_all	67.02	59.02	0.92	84.22	0.92	0.95
	fe2fe3_mix	15.00	13.43	0.94	63.09	0.89	0.89
	fe3_AMD	4.14	4.74	0.78	31.35	0.57	0.59
	goethite_coarse	4.52	4.52	0.85	39.12	0.71	0.74
	goethite_med	2.35	0.76	0.61	56.50	0.23	0.30
Group 2	Kaolin_mix	25.80	18.69	0.85	76.26	0.75	0.80
	mont22	25.72	18.85	0.90	72.21	0.83	0.82
	phyllosilicates	20.53	17.57	0.90	58.26	0.85	0.81
	kaolin_alunite	9.88	9.76	0.90	45.45	0.81	0.85
	kaolgrp	8.53	5.99	0.88	70.53	0.78	0.73
	Alunite_mix	8.03	7.63	0.87	48.58	0.76	0.80
	SiOH	2.34	1.53	0.91	71.70	0.83	0.78
	Na_alunite	1.13	0.68	0.88	63.63	0.75	0.81
	K_alunite	0.68	0.22	0.86	65.67	0.73	0.55
	jarosite	0.31	0.05	0.73	57.41	0.45	0.64
	mont23	0.16	0.04	0.80	56.26	0.59	0.49

Table 2. Endmembers categorized based on high (>50%) or low sensitivity and precision, i.e. which quadrat endmembers appear in Fig 4.

	High sensitivity, high precision	**High sensitivity, low precision**	**Low sensitivity, high precision**	**Low sensitivity, low precision**
Group 1	fe2+generic_carbonate_siderite1 fe2+_chlor+muscphy fe2+_goeth+musc fe3+mix_AMD.assemb1 fe3+_goethite.coarsegr fe3+_goethite.thincoat fe3+_hematite.fine.gr.fe2602 fe3+_hematite.fine.gr.gds76 fe3+_hematite.lg.gr.br34c fe3+_hematite.nano.BR34b2b fe3+_sulfate_jarosite_br34a2 mn2+_rhodonite	fe2+generic_vbroad_br20	fe2+generic_brd.br36a_chlorite fe3+bearing1 fe3+_hematite.lg.gr.br25a fe3+_sulfate_kjarosite200 ree_samarium_oxide	fe2+fe3+mix_with_hematite_br5b fe2+fe3+_chlor+goeth.propylzone fe2+generic_nrw.cummingtonite fe3+_goethite+qtz.medgr.gds240 fe3+_goethite.fingr fe3+_goethite.medcoarsegr.mpc.trjar fe3+_hematite.lg.gr.br25c fe3+_hematite.med.gr.br25b fe3+_hematite.nano.BR34b2
Group 2	Kalun+kaol.intmx Na-alun+kaol.intmx sulfate_alunNa03 sulfate_na40alun400c sulfate+kaolingrp_natroalun+dickite sulfate_alun66K34Na.low sulfate_kalun250c feldspar_buddington.namont2 carbonate_calcite+0.3muscovite calcite+0.2Na-mont carbonate_calcite chlorite-skarn kaolin.5+muscov.medhighAl alunite.5+kaol.5 kaolin+musc.intimat muscovite+chlorite kaolgrp_halloysite kaolgrp_kaolinite_pxl kaolin.5+smect.5 kaol.75+alun.25 kaolin.3+smect.7 smectite_montmorillonite_na_highswelling smectite_beidellite_gds123 smectite_montmorillonite_ca_swelling micagrp_muscovite-medhigh-Al micagrp_muscovite-med-Al micagrp_muscovite-low-Al sioh_chalcedony sioh_hydrated_basaltic_glass	smectite_nontronite_swelling	kaolgrp_dickite sulfate_jarosite-lowT kaolgrp_kaolinite_wxl calcite.25+dolom.25+Na-mont.5	carbonate_calcite+0.2Ca-mont carbonate_dolomite alunite.33+kaol.33+musc.33 carbonate_dolomite.5+Na-mont.5 kaolin.5+muscov.medAl hydroxide_brucite zoisite micagrp_paragonite palygorskite

Table S1. AVIRIS-NG flightline identifiers and URL for reflectance data downloaded from AVIRIS-NG data portal: https://avirisng.jpl.nasa.gov/dataportal/

Flightline	**Spatial Resolution**	**Source URL**
ang20200712t195248	2.8m	https://avng.jpl.nasa.gov/avng/y20_data/ang20200712t202748.tar.gz
ang20200712t200039	2.9m	https://avng.jpl.nasa.gov/avng/y20_data/ang20200712t200039.tar.gz
ang20200712t200729	3.0m	https://avng.jpl.nasa.gov/avng/y20_data/ang20200712t200729.tar.gz
ang20200712t201415	2.9m	https://avng.jpl.nasa.gov/avng/y20_data/ang20200712t201415.tar.gz
ang20200712t202029	2.8m	https://avng.jpl.nasa.gov/avng/y20_data/ang20200712t202029.tar.gz

Figure S1. Median fractional cover in flight area for endmembers detected at AVIRIS-NG scale but not at Tanager scale. Error bars show 25–75% quantile range.